JOURNAL OF SOLID STATE CHEMISTRY **141,** 546–553 (1998)
ARTICLE NO. SC988017

Effects of Cationic Substitution on the Electronic and Magnetic Properties of Manganocuprate with a Layered $Eu_3Ba_2Mn_2Cu_2O_{12}$ Structure

Ichiro Matsubara,*[,1] Noriaki Kida,† Ryoji Funahashi,* Kazuo Ueno,* Hiroshi Ishikawa,* and Nobuhito Ohno†

**Osaka National Research Institute, AIST, Midorigaoka 1, Ikeda, Osaka 563, Japan; and †Osaka Electro Communication University, Hatcho, Neyagawa, Osaka 572, Japan*

Received January 27, 1998; in revised form August 25, 1998; accepted August 31, 1998

Systematic studies on the effect of substitutions on the layered manganocuprate $Eu_3Ba_2Mn_2Cu_2O_{12}$ have been conducted. To introduce holes, we have made substitutions of Ca for Eu and/or Sc for Mn, $(Eu_{3-x}Ca_x)Ba_2(Mn_{2-y}Sc_y)Cu_2O_{12}$. Single-phase compounds are obtained over a fairly wide range of x and y values for $x \le 0.7$ ($y = 0$), $x \le 0.5$ ($y = 0.5$), and $x \le 0.1$ ($y = 1.0$). The doped holes are received predominantly at the Mn–O site and change the charge of Mn from 3+ to 4+, and no superconductivity has been obtained for any sample. The electronic ground state of $(Eu_{3-x}Ca_x)Ba_2(Mn_{2-y}Sc_y)Cu_2O_{12}$ is discussed by comparing with that of the three-dimensional perovskite $La_{1-x}Ca_xMnO_3$ and K_2NiF_4-type $La_{1-x}Sr_{1+x}MnO_4$ compounds. The substitution of Sr for Ba gives rise to a different crystal structure, the $Sr_3Ti_2O_7$ structure. © 1998 Academic Press

1. INTRODUCTION

Since the discovery of high-T_c superconducting cuprates, special attention has been given to layered perovskite oxides consisting of copper oxide layers interleaved between other metal oxide sheets. There are three principal ordered arrangements of B and B' ions in the perovskite oxides of formula $AA'BB'O_6$:BO_6 and $B'O_6$ octahedra are ordered (i) in the NaCl-type of superstructure, (ii) in two directions to yield parallel chains of both octahedra, and (iii) in a layered structure in which two-dimensional BO_6 and $B'O_6$ networks are layered alternatively. The ordering of the B-site cations in a layered structure is a crucial condition for realizing superconductivity. $A_2CuB'O_6$ perovskites tend, however, to show an NaCl type of ordering of Cu and B' (A = La, Sr; B' = W, Nb, Ta, Ir, Sb, Ti) except for the one example of La_2CuSnO_6 with a layered ordering (1–3). In contrast, the introduction of oxygen vacancies leads to the ordering of Cu and B' cations through the formation of ordered oxygen vacancies and different preferences of the cations for octahedral and square-pyramidal coordination. The epoch-making compound $La_2Ba_2Cu_2Sn_2O_{11}$ has been reported by Anderson *et al.* as the first example in which the double layers of square-pyramidal CuO_5 are interleaved with double layers of octahedrally coordinated tin cations (4). The isostructural $Gd_2Ba_2Cu_2Ti_2O_{11}$ has been discovered in the process of systematic substitutional studies in $La_2Ba_2Cu_2Sn_2O_{11}$ (5). Other than these quadruple perovskites, recent publications report new layered cuprates, $Gd_2CaBa_2Ti_2Cu_2O_{12}$ (6), $Y_2Ba_3Cu_3Co_2O_{12}$ (7), $Nd_2Ba_2Ca_mCe_nTi_{2-\delta}Cu_{2+\delta}O_{11+m+2n}$ ($m, n = 0$ or 1) (8), and $Eu_3Ba_2Mn_2Cu_2O_{12}$ (9) with various intergrowth sequences between the sheets of CuO_5 pyramids.

Among these compounds, $Eu_3Ba_2Mn_2Cu_2O_{12}$ is interesting because of its potential for superconductivity but also for magnetoresistance, which appear in hole-doped manganese oxides with the perovskite structure (10–15). $Eu_3Ba_2Mn_2Cu_2O_{12}$ consists of an intergrowth of single rock-salt layers with quadruple oxygen-deficient perovskite layers (Fig. 1). The double layers of CuO_5 square pyramids are, therefore, separated by K_2NiF_4-type layers, instead of double layers of perovskite units. The double layers of square pyramidal CuO_5 units are a familiar structural unit in the oxide superconductors, a new family of potential superconductors. The magnetoresistant properties of these materials depend in a highly sensitive manner on structure (16). In the family of $(La, Sr)_{n+1}Mn_nO_{3n+1}$, perovskite ($n = 1$) compounds show a transition from a high-resistive paramagnetic state to a low-resistive ferromagnetic state upon cooling due to double exchange, the exchange of electrons between Mn^{3+} and Mn^{4+} ions (17). The interaction also causes the giant magnetoresistive effect near the transition temperature. Layered double-perovskite ($n = 2$) compounds exhibit a still larger magnetoresistive effect

---

[1] To whom correspondence should be addressed.

0022-4596/98 $25.00

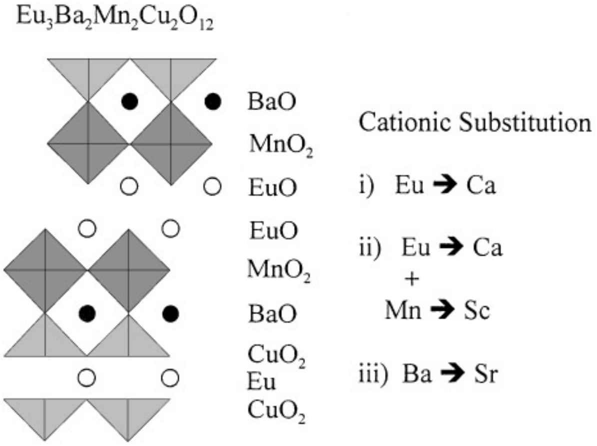

FIG. 1. Schematic diagram of the $Eu_3Ba_2Mn_2Cu_2O_{12}$ structure.

owing to the reduction of dimensionality (16). On the other hand, the two-dimensional K_2NiF_4-type ($n = 1$) compound is not metallic or ferromagnetic (18, 19). In $Eu_3Ba_2Mn_2Cu_2O_{12}$, the K_2NiF_4-type manganate layers are separated by double layers of square-pyramidal cuprate. This compound, therefore, has the further reduced dimensionality of a Mn–O network compared with the simple K_2NiF_4-type compound. It is thus interesting to examine the electronic and magnetic properties of the hole-doped $Eu_3Ba_2Mn_2Cu_2O_{12}$ compounds. In this study, several cationic substitutions have been performed on $Eu_3Ba_2Mn_2Cu_2O_{12}$. To introduce holes, we have made substitutions of Ca for Eu and/or Sc for Mn, $(Eu_{3-x}Ca_x)Ba_2(Mn_{2-y}Sc_y)Cu_2O_{12}$. The stabilization of the $Eu_3Ba_2Mn_2Cu_2O_{12}$ structure as a function of constituent alkaline earth metal, Sr, has been investigated.

2. EXPERIMENTAL

Samples of $(Eu_{3-x}Ca_x)Ba_2(Mn_{2-y}Sc_y)Cu_2O_{12}$ ($0 \leq x \leq 1.0$, $0 \leq y \leq 1.4$) were prepared by conventional solid-state reactions of the appropriate amounts of Eu_2O_3, $CaCO_3$, $BaCO_3$, Mn_2O_3, Sc_2O_3, and CuO. These reactants were mixed thoroughly, pressed into pellets, and then heated at 1000°C for 4 h in air and 1075–1100°C for 4 h with intermediate grinding and pelletizing.

X-ray powder diffraction (XRD) data at room temperature were collected on a Rigaku diffractometer with Cu$K\alpha$ radiation in the range $4^\circ \leq 2\theta \leq 60^\circ$ at an increment of 0.02° (2θ) to examine sample purity and determine cell parameters. Silicon was employed as an internal standard. The temperature-dependent resistivity was measured using a standard four-probe method at a constant dc current of 0.01 mA. The dc magnetization was measured with a superconducting quantum interference device (SQUID) magnetometer ($MPMS_2$: Quantum Design) with a 4-cm scan length in the temperature range 5–300 K. The applied magnetic field was 0.3 T for the M–T measurements. The oxygen content was determined by a melt-reduction method (Horiba EMGA-2800). The pulverized sample was melted in a carbon crucible together with a nickel and tin flux to reduce oxygen to carbon monoxide, which was detected by infrared absorption. Transmission electron microscopy (TEM) images and electron diffraction patterns were obtained with a Hitachi H9000 UHR microscope operated at 300 kV. Samples for TEM observations were prepared using an ion-etching method.

3. RESULTS AND DISCUSSION

A. Eu → Ca Substitution

To introduce holes in the samples, we substituted Ca for Eu, $Eu_{3-x}Ca_xBa_2Mn_2Cu_2O_{12}$ ($0 \leq x \leq 1.0$ in an increment of 0.1). The valence state of the parent compound, $x = 0$, has been reported to be $Eu_3Ba_2Mn^{III}Mn^{IV}Cu_2O_{12}$ (9), and hence there are two possible sites receiving the doped holes, the Cu–O site and/or the Mn–O site. Here we discuss the hole-doping site, change of ground state compared with the cubic and K_2NiF_4-type manganese oxides, and the occurrence of superconductivity.

Figure 2 shows the XRD patterns for samples where $x = 0.0$, 0.6, 0.7, 0.8, 0.9, and 1.0. Because of the

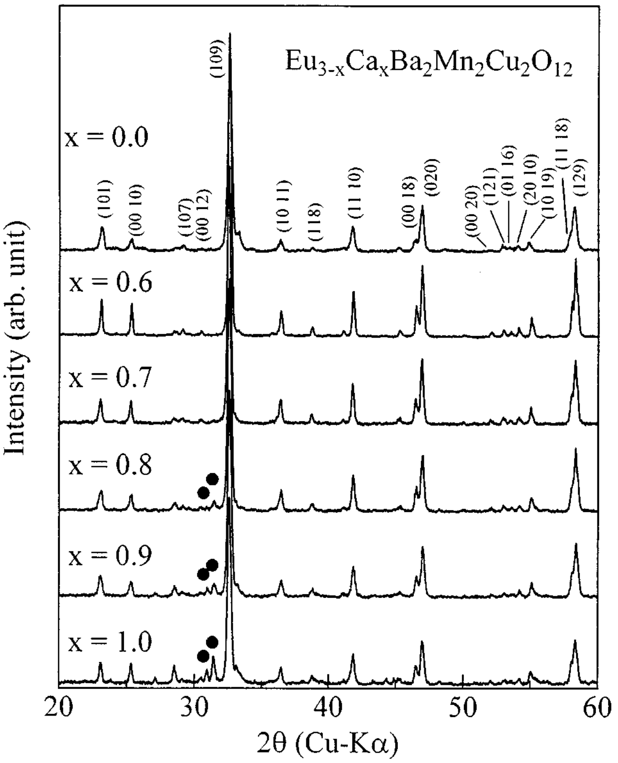

FIG. 2. X-ray diffraction patterns of $Eu_{3-x}Ca_xBa_2Mn_2Cu_2O_{12}$ (x = 0.0, 0.6, 0.7, 0.8, 0.9, and 1.0) indexed on a tetragonal unit cell. Closed circles represent an impurity phase.

improvement of crystallinity, the full width at half-maximum of diffraction peaks is reduced and the intensity of (00*l*) peaks is enhanced for the Ca-substituted samples, reflecting the layered structure. Diffraction peaks due to an impurity phase are marked with closed circles. Although the impurity phase is detected around $2\theta = 31°$ in the $x \geq 0.8$ samples, it is not observed in the $x \leq 0.7$ compounds. All the diffraction peaks of the $x \leq 0.7$ compounds can be indexed on the basis of tetragonal parameters as reported by Hervieu *et al.* (9), indicating that the solid solubility range is $x \leq 0.7$ in the $Eu_{3-x}Ca_xBa_2Mn_2Cu_2O_{12}$ system. The change of lattice parameters is shown as a function of x in Fig. 3. With increasing x, both the *a*- and *c*-axis lattice parameters decrease monotonously, from 3.882 to 3.865 Å and from 35.27 to 35.09 Å, respectively. The lattice parameters of $x = 0.0$ are consistent with those in a previous report (9). They become constant values for the $x \geq 0.8$ samples. The change of the lattice parameters supports the solid solubility range of $x \leq 0.7$ found from the XRD measurements. Such a wide range of solid solubility for the Eu → Ca substitution indicates that $Eu_3Ba_2Mn_2Cu_2O_{12}$ has a large structural flexibility and the capacity to accept holes. On the other hand, the substitution of Ca for the lanthanide in the quadruple perovskites $La_2Ba_2Cu_2Sn_2O_{11}$ and $Gd_2Ba_2Cu_2Ti_2O_{11}$ contains impurity (4, 5).

Figure 4 shows the change of oxygen content measured using a melt-reduction method for the single-phase compounds. The calculated oxygen content in weight percent increases with increasing x because Eu ions are replaced by smaller mass Ca ions. The experimental oxygen content is smaller than the calculated value for all the samples by about 0.3 wt%, indicating the existence of a small amount of oxygen deficiency. However, it increases in the same manner as the calculated value. It should be noted that no extra oxygen deficiency is induced by the Eu → Ca substitution and holes are doped effectively in the $Eu_{3-x}Ca_xBa_2Mn_2Cu_2O_{12}$ compounds.

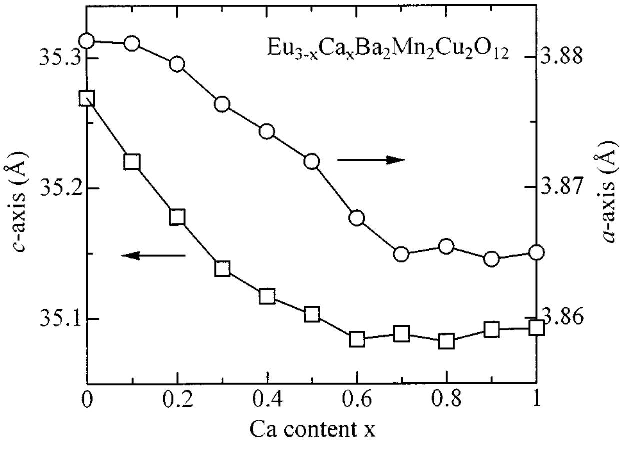

FIG. 3. *a*- and *c*-axis lattice parameters for $Eu_{3-x}Ca_xBa_2Mn_2Cu_2O_{12}$ compounds at room temperature.

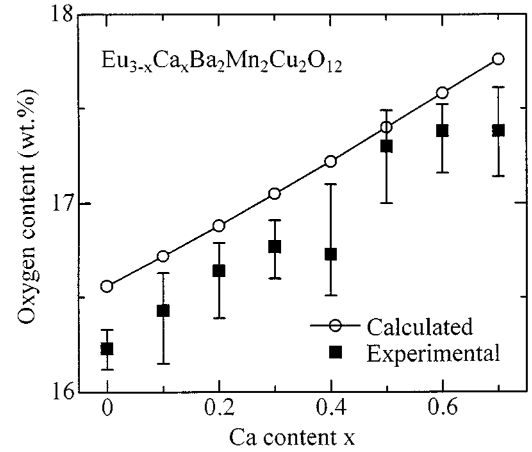

FIG. 4. Calculated (open circles) and experimental (closed squares) oxygen content of $Eu_{3-x}Ca_xBa_2Mn_2Cu_2O_{12}$ compounds.

We can identify whether the doped holes are present at the Cu–O site or the Mn–O site from the result of the lattice parameter changes because of the substitution. In the $La_{1-x}Sr_{1+x}MnO_4$ ($0.5 < x < 1.0$) system with the K_2NiF_4 structure, the *a*-axis decreases with x (19, 20), whereas it has been reported that the *c*-axis increases slightly (19) or decreases (20). In the case of the *c*-axis, the effect of the increasing value caused by the substitution of the larger Sr ions for La ions and the effect of the decreasing value caused by the change in charge of Mn ions from 3.5+ ($x = 0.0$) to 4+ ($x = 0.5$) may balance out. In the case of the $Eu_{3-x}Ca_xBa_2Mn_2Cu_2O_{12}$ system, because the difference in ionic radii between Eu^{3+} and Ca^{2+} is much smaller than that between the La^{3+} and Sr^{2+} ions, both the *a*- and *c*-axis would be predicted to decrease with Ca content when the holes are present at the Mn–O site. It has been reported that the in-plane Cu–O bond length decreases and the apical Cu–O bond length increases in the CuO_5 pyramid when holes are doped in the CuO_2 plane (21). If the holes, were doped at the Cu–O site, *a*- and *c*-axis values would decrease and increase, respectively, in the $Eu_{3-x}Ca_xBa_2Mn_2Cu_2O_{12}$ system. The change of lattice parameters (Fig. 3) strongly suggests that the doped holes due to the Eu → Ca substitution are at the Mn–O site, which is reasonable considering the higher 3*d* energy level of Mn than Cu.The increase of Ca content from $x = 0.0$ to $x = 0.7$ corresponds to the change in the formal charge of Mn from 3.5+ to 3.85+ assuming the $Eu_{3-x}Ca_xBa_2Mn_2Cu_2O_{12}$ oxygen stoichiometry.

Magnetization was measured as a function of temperature and field. The magnetization M vs temperature T plot measured in a zero-field-cooled (ZFC) sequence is shown in Fig. 5. There is a magnetic transition at temperatures lower than 30 K, where a steep increase in M is observed. In the

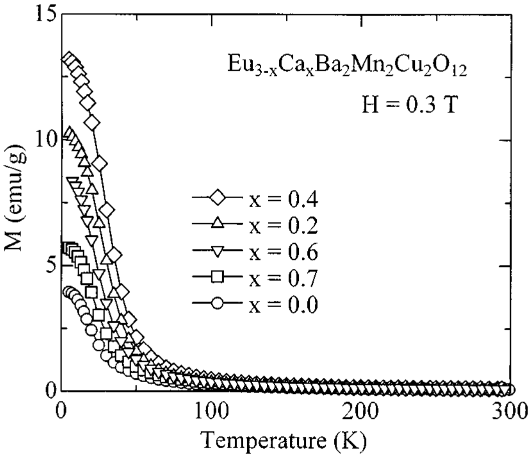

FIG. 5. Magnetization vs temperature plot for $Eu_{3-x}Ca_xBa_2Mn_2Cu_2O_{12}$ ($x = 0.0$, 0.2, 0.4, 0.6, and 0.7) measured in a field of 0.3 T.

magnetization M vs applied field H curve, a distinct hysteresis cycle is observed at 5 K, indicating that the magnetic transition is due to the ferromagnetic ordering as reported by Hervieu *et al.* (9). They have reported another magnetic ordering at 100 K, whereas such a distinct transition was not observed in our measurements. The ferromagnetic moment at 5 K increases with increasing Ca content up to $x = 0.4$ and decreases again to a similar value in the undoped $x = 0.0$ compound. The inverse magnetic susceptibility vs temperature plot is analyzed according to a Curie–Weiss law, $\chi = C/(T - \Theta)$, where C is the Curie constant and Θ is the paramagnetic Curie temperature. The effective paramagnetic moment $\mu_{\rm eff}$ is estimated from the Curie constant. The $\mu_{\rm eff}$ and Θ values are summarized in Table 1 together with the ferromagnetic transition temperature ($T_{\rm F}$) and remanent magnetization (I_r). The $\mu_{\rm eff}$ values are in the range 8.6–9.1 μ_B. These values agree with those calculated using the moments of 3.4 $\mu_{\rm B}$ for Eu^{3+}, 4 $\mu_{\rm B}$ for Mn^{4+}, 5.1 $\mu_{\rm B}$ for Mn^{3+}, and 2.4 $\mu_{\rm B}$ for Cu^{2+}, 8.5–9.4 $\mu_{\rm B}$, depending on the Mn^{3+}/Mn^{4+} ratio. The obtained $T_{\rm F}$, Θ, and I_r indicate that the ferromagnetic interaction is most marked for the $x = 0.3$ and 0.4 compounds.

All the compounds show a semiconducting-like transport ($d\rho/dT < 0$) as in the case of $La_{1-x}Sr_{1+x}MnO_4$ compounds. The resistivity monotonously decreases with increasing Ca content. The resistivity at room temperature drops by about two orders of magnitude for the $x = 0.7$ sample compared to the undoped $x = 0.0$ one. This tendency can be contrasted with that in the $La_{1-x}Sr_{1+x}MnO_4$ ($0.5 < x < 0.7$) system, in which resistivity at room temperature increases with increasing x, corresponding to the increase of Mn^{4+} (18). The $La_{1-x}Sr_{1+x}MnO_4$ ($0.5 < x < 0.7$) compounds have an anomaly around 230 K, where the R–T curve shows a steep increase due to real-space ordering of the doped holes (18). There is no such anomalous behavior in any $Eu_{3-x}Ca_xBa_2Mn_2Cu_2O_{12}$ compound.

TABLE 1
Magnetic Propeties of $Eu_{3-x}Ca_xBa_2Mn_2Cu_2O_{12}$

Sample (x)	$\mu_{\rm eff}$[a] (μ_B)	Θ (K)[b]	$T_{\rm F}$ (K)[c]	$I_{\rm r}$ (emu/g)[d]
0.0	8.8	1.0	19	0.1
0.1	9.0	20.2	24	0.5
0.2	8.7	30.1	30	1.9
0.3	8.6	38.3	34	1.8
0.4	9.1	38.8	32	1.5
0.5	8.7	36.2	29	1.2
0.6	8.9	25.6	26	0.7
0.7	8.7	25.4	22	0.2

[a] Effective paramagnetic moment.
[b] Paramagnetic Curie temperature.
[c] Ferromagnetic transition temperature.
[d] Remanent magnetization.

A plot of resistivity vs T^{-1} shows a continuous decreasing slope with T (Fig. 6a). The logarithm of the resistivity is plotted against $T^{-1/4}$ in Fig. 6b to illustrate the agreement between the data and the Mott variable-range-hopping (VRH) low, $\rho = \rho_0(T/T_0)^{1/2}\exp((T_0/T)^{1/(d+1)})$, where ρ_0 is a virtually temperature-independent material parameter, T_0 is a measure for the degree of charge carrier localization, and d is the dimension of the conduction mechanism (22). A $T^{-1/4}$ dependence would be consistent with the isotropic conductivity although a $T^{-1/3}$ dependence would be expected from the layered structure. It is difficult to determine experimentally which dependence is provable for the polycrystalline samples. The quantity $K_{\rm B}T_0$ is related to the density of state at the Fermi energy $g(E_{\rm F})$ and the localization length ξ as $K_{\rm B}T_0 \cong \beta/g(E_{\rm F})\xi^3$, where $K_{\rm B}$ is the Boltzmann constant. The T_0 values obtained by least-squares fitting of the data are 4.2×10^8, 2.7×10^8, 1.8×10^8, and 1.4×10^8 K for the $x = 0.0$, 0.3, 0.5, and 0.7 compounds, respectively. The $T^{-1/4}$ dependence cannot be followed to very low temperatures because the values of T_0 are so large, being consistent with those of amorphous semiconductors (23), that the resistivity quickly becomes too large to measure as T is reduced. Assuming that ξ is $\sim$10 Å (24), $g(E_{\rm F})$ is estimated to be on the order of $10^{20}/\text{cm}^3$ eV, and the decrease of resistivity with Ca content could be attributed to the increase of $g(E_{\rm F})$.

The electronic phase diagram of $Eu_{3-x}Ca_xBa_2Mn_2Cu_2O_{12}$ as a function of x is given in Fig. 7 together with those of $La_{1-x}Ca_xMnO_3$ (25) and $La_{1-x}Sr_{1+x}MnO_4$ (18). Comparing the diagram of these three compounds, we can consider the effect of Mn–O network dimensionality on electromagnetic properties in the range between $Mn^{4+}/(Mn^{3+} + Mn^{4+}) = 50\%$ and 85%. It is concluded that $Eu_{3-x}Ca_xBa_2Mn_2Cu_2O_{12}$ has a ground state of a ferromagnetic insulator (FM-I). There is no evidence of charge ordering. The spin-glass state due to the competition between the generic antiferromagnetic superexchange

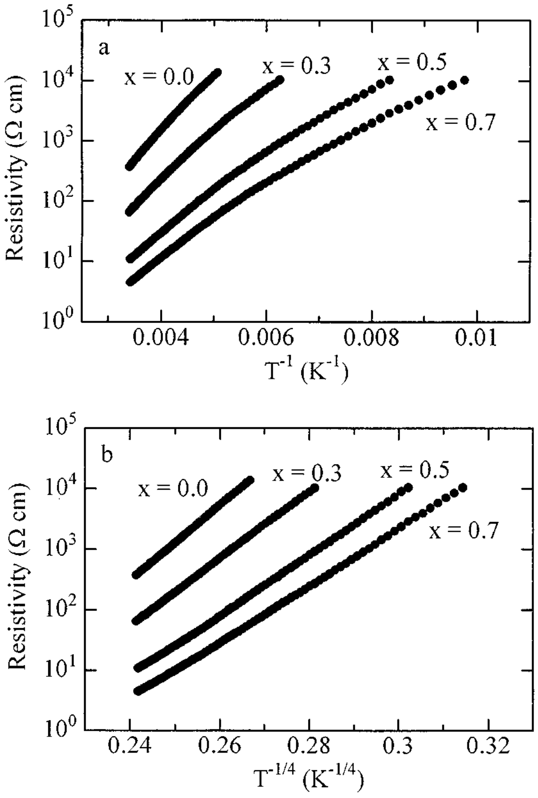

FIG. 6. Plot of resistivity vs T^{-1} (a) and $T^{-1/4}$ (b) for $Eu_{3-x}Ca_xBa_2Mn_2Cu_2O_{12}$ ($x = 0.0$, 0.3, 0.5, and 0.7).

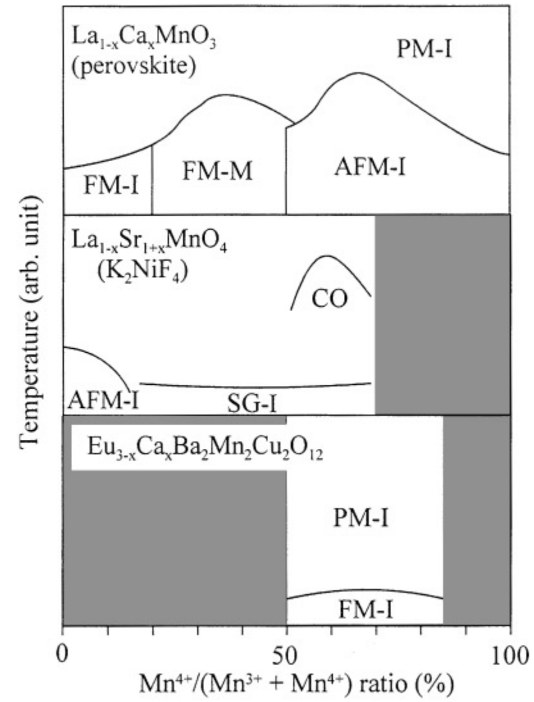

FIG. 7. Electronic phase diagrams of $Eu_{3-x}Ca_xBa_2Mn_2Cu_2O_{12}$, $La_{1-x}Ca_xMnO_3$ (25), $La_{1-x}Sr_{1+x}MnO_4$ (18). FM, AFM, PM, SG, CO, -M, and -I stand for ferromagnetic, antiferromagnetic, paramagnetic, spin glass, charge ordering, metal, and insulator, respectively.

interaction and the ferromagnetic double-exchange interaction has been observed for $La_{1-x}Sr_{1+x}MnO_4$. Basically, all three compounds are thought to have two magnetic interactions which are reduced by increasing the two-dimensionality. The $La_{1-x}Ca_xMnO_3$ compounds clearly show an antiferromagnetic transition in the magnetization vs temperature curve at temperatures higher than $T_N = 150$ K, whereas it is not observed for $Eu_{3-x}Ca_xBa_2Mn_2Cu_2O_{12}$. In the anisotropic magnetization measurements for $LaSrMnO_4$ single crystal, an antiferromagnetic transition is observed at 120 K only for $H//c$-axis configuration, indicating that the behavior is characteristic of an antiferromagnetic transition with spins aligned along the c-axis (18). This has been supported by neutron diffraction results (26). The antiferromagnetic interaction is therefore drastically reduced by increasing the two-dimensionality, especially for $Eu_{3-x}Ca_xBa_2Mn_2$ Cu_2O_{12}. The paramagnetic Curie temperature θ for $Eu_3Ba_2Mn_2Cu_2O_{12}$, $La_{0.5}Sr_{1.5}MnO_4$, and $La_{0.5}Ca_{0.5}$ MnO_3 is 1, 310, and 312 K, respectively. The decrease of Θ also suggests a reduction of ferromagnetic interaction. However, the degree of reduction is very significant for an antiferromagnetic interaction, indicating that the ground state of $Eu_{3-x}Ca_xBa_2Mn_2Cu_2O_{12}$ is that of a ferromagnetic insulator.

B. (Mn → Sc) + (Eu → Ca) Substitution

Evidence of superconductivity has not been observed in the $Eu_{3-x}Ca_xBa_2Mn_2Cu_2O_{12}$ compounds because the doped holes are predominantly at the Mn–O site. To try to dope holes into the CuO_2 plane, we have prepared $(Eu_{3-x}Ca_x)Ba_2(Mn_{2-y}Sc_y)Cu_2O_{12}$, in which the mixed-valence Mn ions are substituted by Sc ions with a fixed charge of 3+ .

Figure 8 shows the solid solubility range for $(Eu_{3-x}Ca_x)Ba_2(Mn_{2-y}Sc_y)Cu_2O_{12}$. There is no detectable impurity phase in the XRD pattern for $y \leq 1.0$ when $x = 0.0$, corresponding to the abscissa line in Fig. 8. The change of lattice parameters of $Eu_3Ba_2(Mn_{2-y}Sc_y)Cu_2O_{12}$ is shown as a function of y in Fig. 9. Both the a- and c-axis lattice parameters increase monotonously from 3.885 to 3.913 Å and from 35.26 to 35.70 Å with substitution, which reflects the difference in ionic radii of the Mn and Sc ions. The lattice parameters become constant values for the $x > 1.0$ samples. The change of lattice parameters supports the solid solubility range of $y \leq 1.0$ determined from XRD measurements. The amount of substitution of Sc for Mn reaches as high as Sc/(Mn + Sc) = 50%.

Magnetization of $Eu_3Ba_2(Mn_{2-y}Sc_y)Cu_2O_{12}$ was measured as a function of temperature and field. The

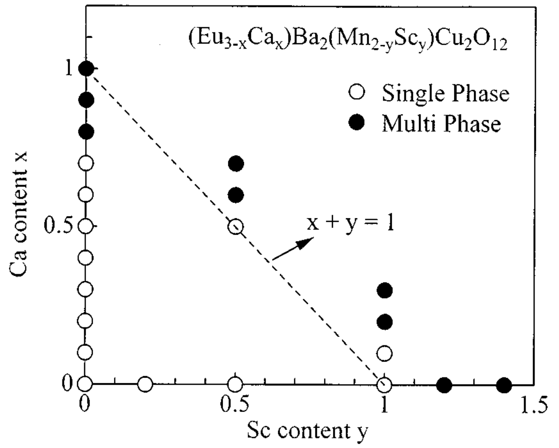

FIG. 8. Solid solubility range for $(Eu_{3-x}Ca_x)Ba_2(Mn_{2-y}Sc_y)Cu_2O_{12}$.

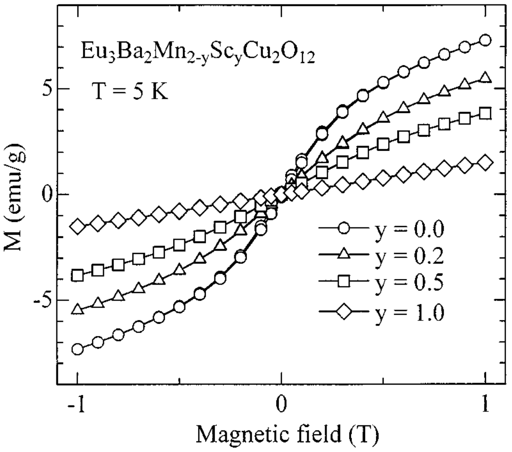

FIG. 10. Magnetization vs applied field curves for $Eu_3Ba_2(Mn_{2-y}Sc_y)Cu_2O_{12}$($y = 0.0$, 0.2, 0.5, and 1.0) measured at 5 K.

ferromagnetic transition clearly observed for the $y = 0.0$ sample disappears with increasing y up to 1.0. The magnetization M vs applied field H curve is shown in Fig. 10; the distinct hysteresis cycle vanishes and it is replaced by paramagnetic behavior with increasing y. The ferromagnetic interaction is thought to be reduced due to the incorporation of a foreign ion, Sc^{3+}, in the pure Mn–O network. These results imply that the observed magnetic behavior in the $y = 0.0$ samples is derived mainly from the K_2NiF_4-type Mn–O layers.

As the charge of Sc is fixed at 3 +, hole doping into the CuO_2 plane is expected when the total amount of ($Ca \rightarrow Eu + Sc \rightarrow Mn$) substitution is larger than one, $x + y > 1$. In the pure samples shown in Fig. 8, the ($x = 0.1$, $y = 1.0$) sample satisfies the condition of $x + y > 1$. Figure 11 shows the temperature dependence of the resistivity of the ($x = 0.1$, $y = 1.0$) sample compared with the ($x = 0.0$, $y = 1.0$) sample. Although the resistivity decreases by about one order of magnitude due to the Eu → Ca substitution, it is still semiconducting. The results of oxygen analysis of the ($x = 0.1$, $y = 1.0$) sample indicate an oxygen deficiency of $\delta = 0.1$ in the chemical formula, $(Eu_{2.9}Ca_{0.1})Ba_2(Mn_{1.0}Sc_{1.0})Cu_2O_{12-\delta}$. The actual doped holes are, therefore, less than those which are expected to be doped into the CuO_2 plane. It should be mentioned that the substitution of Sc for Mn may induce disordering in the B-site cations. A neutron diffraction study is necessary to investigate the change in the ordered structure. The CuO_2 plane seems to hardly receive the doped holes in the $(Eu_{3-x}Ca_x)Ba_2(Mn_{2-y}Sc_y)Cu_2O_{12}$ compounds.

C. Ba → Sr Substitution

The in-plane Cu–O bond length estimated from the lattice constant is 1.94–1.96 Å, which is larger than that of

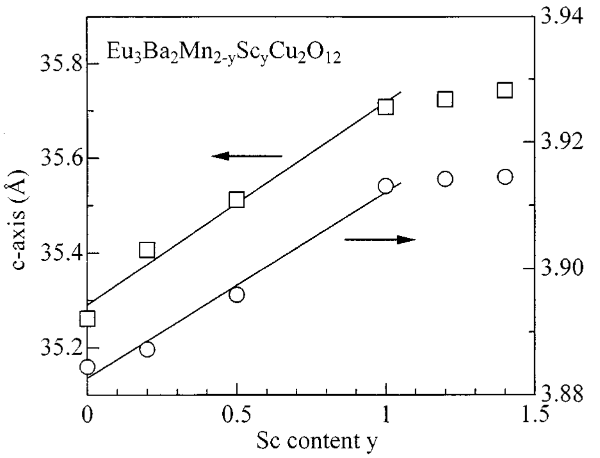

FIG. 9. a- and c-axis lattice parameters for compounds at room temperature.

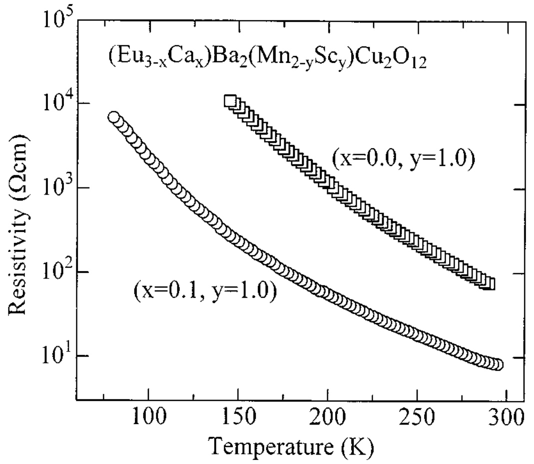

FIG. 11. Temperature dependence of resistivity of ($x = 0.0$, $y = 1.0$: open squares) and ($x = 0.1$, $u = 1.0$: open circles) compounds.

typical p-type superconductors and, if anything, closer to that of n-type superconductors. This would explain the lack of superconductivity in doped $Eu_3Ba_2Mn_2Cu_2O_{12}$ compounds. Attempts to dope electrons into this material with tetravalent Ce ions on the Eu sites failed to produce a single-phase compound. To shorten the the in-plane Cu–O bond length, the substitution of Sr for Ba was attempted.

The stoichiometric composition $Eu_3Sr_2Mn_2Cu_2O_z$ has a structure different from the $Eu_3Ba_2Mn_2Cu_2O_{12}$ structure. Figure 12 shows the powder XRD patterns of these two samples. Almost all the diffraction peaks of the $Eu_3Sr_2Mn_2Cu_2O_z$ compound can be indexed on the basis of a tetragonal unit cell with $a = 3.79$ Å and $c = 20.3$ Å. Some small peaks due to an impurity phase are observed (shown by closed circles in Fig. 12). It is important to select the proper lanthanides to obtain pure layered copper perovskites (27, 28). The $Ln_3Sr_2Mn_2Cu_2O_z$ (Ln = Nd, Gd) compounds prepared under the same conditions as $Eu_3Sr_2Mn_2Cu_2O_z$ show an impurity phase in their XRD pattern. Attempts to synthesize a pure phase by substituting constituent lanthanides for Eu were unsuccessful. Efforts to determine the composition and optimal processing conditions for the single phase were concentrated on $Gd_3Sr_2Mn_2Cu_2O_z$. Attempts to improve the phase purity were made by slightly varying starting compositions of Gd, Sr, and Cu. The mixtures of starting materials were heated at various temperatures (1050–1150°C) for 30–60 h. Among these samples, the off-stoichiometric $Gd_{2.5}Sr_{2.2}Mn_2Cu_{2.1}O_z$ compound heated at 1050°C for 30 h shows no impurity phases in its XRD pattern.

From the XRD patterns and cell parameters, we propose the $Sr_3Ti_2O_7$ structure, the second member of the Ruddlesden–Popper-type compound series, as the structural model for $Gd_{2.5}Sr_{2.2}Mn_2Cu_{2.1}O_z$. This model is supported by TEM observations. Figure 13 shows a high-resolution transmission electron microscope image with the incident electron beam along the [110] direction and the corresponding selected-area electron diffraction pattern. The lattice image clearly shows layers with a uniform spacing of about 10 Å, which corresponds to nearly half the c-axis unit length. There is no stacking fault in this observation, indicating a high homogeneity in this layered compound. The electron diffraction pattern can be indexed with respect to the $(a^* + b^*) - c^*$ reciprocal lattice sections of the tetragonal cell with $a = b = 3.8$ and $c = 20$ Å. The layer spacing and the observed atomic image strongly support the $Sr_3Ti_2O_7$ structure. Detailed structural analysis is now in progress.

Considering the structural model, the $Gd_{2.5}Sr_{2.2}Mn_2Cu_{2.1}O_z$ compound has a large deficiency in the A-site cations (Gd + Sr). The stoichiometric composition would be expected to be $(Gd,Sr)_6(Mn,Cu)_4O_{14}$. The a-axis cell parameter of $Gd_{2.5}Sr_{2.2}Mn_2Cu_{2.1}O_z$ is smaller than that of isostructural $LaSr_2Mn_2O_7$ (20) and $Ca_3Ru_2O_7$ (29), which is caused by the large cation deficiency. When the $Gd_{2.5}Sr_{2.2}Mn_2Cu_{2.1}O_z$ compound has the ordered structure in which the Mn double perovskite units and the Cu oxygen-deficient double perovskite units are stacked alternately, layers with a different spacing should be observed alternately. This is not the case in our TEM observation, in which a very uniform spacing of 10 Å is found in each layer. This indicates that the B-site cations, Mn and Cu ions, may be disordered in $Gd_{2.5}Sr_{2.2}Mn_2Cu_{2.1}O_z$ with the $Sr_3Ti_2O_7$ structure. The susceptibility obeys Curie–Weiss behavior

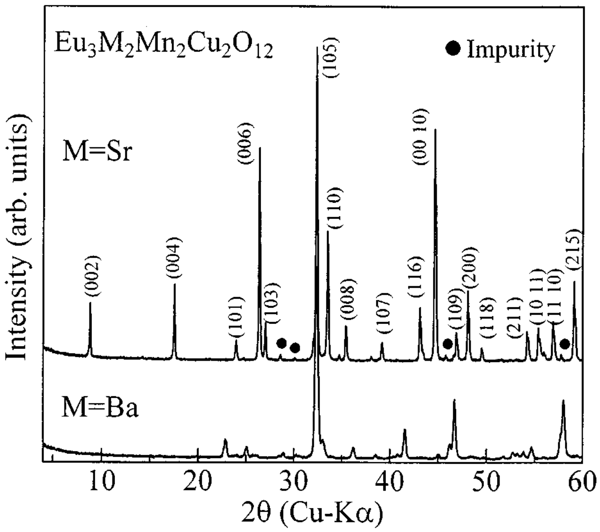

FIG. 12. X-ray diffraction pattern of $Eu_3Sr_2Mn_2Cu_2O_z$ compared with that of $Eu_3Ba_2Mn_2Cu_2O_{12}$. Closed circles show an impurity phase.

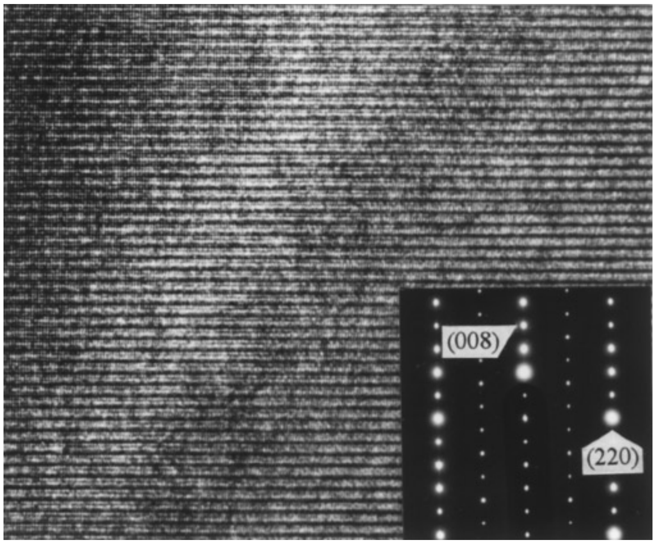

FIG. 13. High-resolution transmission electron microscope image with incident electron beam along the [110] direction and corresponding selected-area electron diffraction pattern for $Gd_{2.5}Sr_{2.2}Mn_2Cu_{2.1}O_z$.

over a wide temperature range. The temperature dependence of the resistivity exhibits a semiconductive behavior. The apparent lack of magnetic ordering and the high resistivity are attributed to the *B*-site cation disordering.

The substitution of Sr for Ba in $Eu_3Ba_2Mn_2Cu_2O_{12}$ gives rise to a change in the stable phase and the disappearance of *B*-site cation ordering. In our previous study on the stability of $Ln_3Ba_2Mn_2Cu_2O_{12}$ (Ln = Nd, Sm, Eu, Gd, Tb, Dy, Er, Yb), we have reported that the $Eu_3Ba_2Mn_2Cu_2O_{12}$ structure is stabilized by a particular ionic size at the *Ln* site (Ln = Sm, Eu, Gd) (30). Selection of proper *A*-site cations, lanthanide and alkaline earth cations, is a crucial condition for obtaining the $Eu_3Ba_2Mn_2Cu_2O_{12}$ structure.

4. CONCLUSION

We have prepared solid solutions in the $(Eu_{3-x}Ca_x)Ba_2(Mn_{2-y}Sc_y)Cu_2O_{12}$ system. Single-phase compounds are obtained in a fairly wide range of x and y values for $x \leq 0.7$ ($y = 0$), $x \leq 0.5$ ($y = 0.5$), and $x \leq 0.1$ ($y = 1.0$). We have obtained some evidence for successful doping of holes through the substitution. The doped holes are received dominantly at the Mn–O site and change the average charge of Mn from 3.5+ to 3.85+. Superconductivity is not observed in the $(Eu_{3-x}Ca_x)Ba_2(Mn_{2-y}Sc_y)Cu_2O_{12}$ system. The CuO_2 plane accepts almost no holes in the layered manganocuprates. The ground state of the $Eu_{3-x}Ca_xBa_2Mn_2Cu_2O_{12}$ compounds is that of a ferromagnetic insulator. The substitution of Sc for Mn causes the disappearance of the ferromagnetic interaction, indicating that the interaction comes from the Mn–O layers. The substitution of Sr for Ba induces a different crystal structure, the $Sr_3Ti_2O_7$ structure, together with the disordering of the *B*-site cations. Single-phase compounds are obtained from the nominal composition of $Gd_{2.5}Sr_{2.2}Mn_2Cu_{2.1}O_z$, which implies a large *A*-site cation deficiency.

REFERENCES

1. F. S. Galasso, "Perovskites and High T_c Superconductors." Gordon & Breach, New York, 1990.
2. P. Gómez-Romero, M. R. Palacín, N. Casañ, A. Fuertes, and B. Martínez, Solid State Ionics **63–65,** 603 (1993).
3. M. T. Anderson and K. R. Poeppelmeier, *Chem. Mater.* **3,** 476 (1991).
4. D. T. Anderson, K. R. Poeppelmeier, J.-P. Zhang, H.-J. Fan, and L. D. Marks, *Chem. Mater.* **4,** 1305 (1992).
5. A. Gormezano and M. T. Weller, *J. Mater. Chem.* **3,** 771 (1993).
6. A. Fukuoka, S. Adachi, T. Sugano, X.-J. Wu, and H. Yamauchi, *Physica C* **231,** 372 (1994).
7. W. Zhou and D. A. Jefferson, *J. Solid State Chem.* **115,** 407 (1995).
8. T. Den, T. Kobayashi, F. Izumi, T. Kamiyama, Y. Shimakawa, J. D. Jorgensen, F. J. Rotella, and R. L. Hitterman, *Physica C* **255,** 37 (1995).
9. M. Hervieu, C. Michel, R. Genouel, A. Maignan, and B. Raveau, *J. Solid State Chem.* **115,** 1 (1995).
10. K. Chahara, T. Ohno, M. Kasai, and Y. Kozono, *Appl. Phys. Lett.* **63,** 1990 (1993).
11. R. Van Helmolt, J. Wecker, B. Holzapfel, L. Schultz, and K. Samwer, *Phys. Rev. Lett.* **77,** 2331 (1993).
12. Y. Tokura, A. Urushibara, Y. Moritomo, T. Arima, A. Asamitsu, G. Kido, and N. Furukawa, *J. Phys. Soc. Jpn.* **63,** 3931 (1994).
13. S. Jin, T. H. Tiefel, M. McCormack, R. A. Fastnacht, R. Ramesh, and L. H. Chen, *Science* **264,** 413 (1994).
14. H. L. Ju, J. Gopalakrishnan, J. L. Peng, Q. Li, G. C. Xiong, T. Venkatesan, and R. L. Greene, *Phys. Rev. B* **51,** 6143 (1995).
15. A. Urushibara, Y. Moritomo, T. Arima, A. Asamitsu, G. Kido, and Y. Tokura, *Phys. Rev. B* **51,** 14103 (1995).
16. Y. Moritomo, A. Asamitsu, H. Kuwabara, and Y. Tokura, *Nature* **380,** 141 (1996).
17. C. Zener, *Phys. Rev.* **82,** 403 (1951).
18. Y. Moritomo, Y. Tomioka, A. Asamitsu, Y. Tokura, and Y. Matsui, *Phys. Rev. B* **51,** 3297 (1995).
19. W. Bao, C. H. Chen, S. A. Carter, and S.-W. Cheong, *Solid State Commun.* **98,** 55 (1996).
20. R. A. H. Ram, P. Ganguly, and C. N. R. Rao, *J. Solid State Chem.* **80,** 82 (1987).
21. S. Kanbe, K. Kishio, K. Kitazawa, K. Fueki, H. Takagi, and S. Tanaka, *Chem. Lett.* 547 (1987).
22. N. F. Mott, *Philos. Mag.* **19,** 835 (1969).
23. M. L. Knotek and M. Pollak, *Phys. Rev. B* **9,** 664 (1974).
24. M. A. Kastber, R. J. Birgeneau, C. Y. Chen. Y. M. Chiang, D. R. Gabbe, H. P. Jenssen, T. Junk, C. J. Peters, P. J. Picone, T. Thio, T. R. Thurston, and H. L. Tuller, *Phys. Rev. B* **37,** 111 (1988).
25. P. Schiffer, A. P. Ramirez, W. Bao, and S. W. Cheong, *Phys. Rev. Lett.* **75,** 3336 (1995).
26. S. Kawano, N. Achiwa, N. Kamegasira, and M. Aoki, *J. Phys., Colloq.* **49,** 829 (1988).
27. P. Gómez-Romero, M. R. Palacín, and J. Rodríguez-Carvajal, *Chem. Mater.* **6,** 2118 (1994).
28. K. V. Greenwood, G. M. Sarjeant, K. R. Poeppelmeier, P. A. Salvador, T. O. Mason, B. Dabrowski, K. Rogacki, and Z. Chen, *Chem. Mater.* **7,** 1335 (1995).
29. G. Gao, S. McCall, J. E. Crow, and R. P. Guertin, *Phys. Rev. Lett.* **78,** 1751 (1997).
30. I. Matsubara, R. Funahashi, N. Kida, and K. Ueno, *Chem. Lett.* 971 (1996).